



HAL
open science

Solidus melting of pyrolite and bridgmanite: Implication for the thermochemical state of the Earth's interior

Rémy Pierru, Laure Pison, Antoine Mathieu, Emmanuel Gardés, Gaston Garbarino, Mohamed Mezouar, Louis Hennet, Denis Andrault

► To cite this version:

Rémy Pierru, Laure Pison, Antoine Mathieu, Emmanuel Gardés, Gaston Garbarino, et al.. Solidus melting of pyrolite and bridgmanite: Implication for the thermochemical state of the Earth's interior. *Earth and Planetary Science Letters*, 2022, 595, pp.117770. 10.1016/j.epsl.2022.117770 . hal-03759424

HAL Id: hal-03759424

<https://hal.science/hal-03759424>

Submitted on 21 Nov 2022

HAL is a multi-disciplinary open access archive for the deposit and dissemination of scientific research documents, whether they are published or not. The documents may come from teaching and research institutions in France or abroad, or from public or private research centers.

L'archive ouverte pluridisciplinaire **HAL**, est destinée au dépôt et à la diffusion de documents scientifiques de niveau recherche, publiés ou non, émanant des établissements d'enseignement et de recherche français ou étrangers, des laboratoires publics ou privés.

Solidus melting of pyrolite and bridgmanite: implication for the thermochemical state of the Earth's interior

Rémy PIERRU¹, Laure PISON¹, Antoine MATHIEU¹, Emmanuel GARDES^{1,2}, Gaston GARBARINO³, Mohamed MEZOUAR³, Louis HENNET⁴ and Denis ANDRAULT^{1,£}

¹ Université Clermont Auvergne, LMV, CNRS-OPGC-IRD, Clermont-Ferrand, France

² Normandie Université, ENSICAEN, CEA, CNRS, CIMAP, Caen, France

³ European Synchrotron Radiation Facility, Grenoble, France

⁴ Université d'Orléans, ICMN, CNRS, Orléans, France

£ Corresponding author

Abstract

Melting properties of the deep mantle remain controversial due to experimental difficulties; e.g., reports of solidus temperatures of mantle-relevant compositions span over ~700K at 2000 km depth. This situation limits our understanding of the thermochemical state of the Earth's interior. Using the laser heated diamond anvil cell (LH-DAC), we performed new experimental determination of the solidus profile of ultra-dry pyrolite and the solidus of two compositions of (Mg,Fe)(Si,Al)O₃ bridgmanite (Bg). Melting was detected (i) from -the correlation between laser power and sample temperature, -changes of sample texture and -the level of visible light absorption, for all samples, (ii) using X-ray diffraction, for the MgSiO₃ composition and (iii) after scanning electron microscope observations, for selected Fe-bearing samples. Special care was given to using ultra-dry experimental chambers and to determination of sample temperature. In particular, we discuss the wavelength-dependent thermal emission of silicate samples, which lowers the solidus by 100 to 300K, compared to the grey-body assumption.

The solidus of MgSiO₃-Bg is in good agreement with previous reports using *ab initio* calculations and shock wave experiments. We observe a net decrease in the solid-liquid Clapeyron slope at 60(3) GPa and 4400(200) K, which can be related to rapid pressure-induced coordination change of Si in the melt. (Mg_{0.955},Fe_{0.045})(Si_{0.993},Al_{0.007})O₃ Bg melts 600-800 K lower than MgSiO₃-Bg. Its solidus evolves smoothly with pressure, suggesting progressive Si coordination change in the melt. In the pressure range investigated (24-135 GPa) Clapeyron slopes suggest rapid decrease of the volume of fusion, from 14 to 2% for MgSiO₃ and from 9 to 3% for (Fe,Al)-bearing Bg, assuming congruent melting. By comparing the solidii of various silicates, it appears that the higher the number of cations, the less pronounced is the curvature of the solidus. This observation suggests that the relatively ordered structure of simple liquid compositions with a limited number of distinct network-modifying cations frustrates the coexistence of tetrahedrally and octahedrally coordinated Si polyhedral.

The solidus of pyrolite presents a smooth evolution from 2200(100) K to 3950(200) K in the same pressure interval. This is very similar to our previous work on chondritic-type mantle. The new solidus is 200-300 K lower than that of KLB-1 peridotite, which can be related to more incompatible elements in pyrolite. It remains problematic that our solidus plots several 100 K higher than other recent measurements performed on pyrolite; we discuss the possibility of a higher water content in previous samples, compared to our experiments. Assuming a dry lowermost mantle, our results imply a core-mantle boundary temperature lower than 3950(200) K. Modeling the melting diagram at the core-mantle boundary suggests a pseudo-eutectic melt significantly depleted in SiO₂, compared to the composition of the mean mantle.

Highlights:

- Mantle solidus evolves from 2200(100) and 3950(200) K with depth in lower mantle
- Solidus of pyrolite suggests core-mantle boundary temperature lower than 3950(200)K
- The initially steep solidus of MgSiO₃ bridgmanite flattens at 60(3) GPa
- Silicate melts with more cations present smooth solidus evolution to CMB pressure

56 Introduction

57

58 Earth is very hot inside due to the major Moon forming impact that occurred 50-100 million years after
59 its accretion. The impact melted its interior almost entirely (Nakajima and Stevenson, 2015). For this reason,
60 mantle melting contributed largely to the internal dynamics of the Earth during its history. It is believed that
61 partial melting is still occurring today in specific mantle regions such as in the ultra-low velocity zones
62 (ULVZ) atop the core-mantle boundary (CMB; e.g. (Lay et al., 2004)) and the low-velocity layer between
63 350 and 410 km depth (LVL; e.g. (Tauzin et al., 2010)). Knowledge of the melting properties in the deep
64 mantle is key to refine our knowledge of mantle history. In this work, we limit our analysis to the
65 determination of the mantle solidus at lower mantle conditions.

66 There are not many reports on deep mantle melting, due to experimental and theoretical difficulties
67 associated with (i) the very high pressure involved, up to 135 GPa at the core-mantle boundary (CMB), and
68 (ii) the composition of the mantle which includes many elements. *Ab initio* calculations can be used to
69 estimate the solidii of pure phases, such as MgSiO₃ bridgmanite (Bg) (Stixrude et al., 2009); However, it
70 remains difficult to model the melting properties of more complex geological material. Similar limitation
71 occurs for shock wave experiments, for which it is difficult to investigate a mixture of phases. Another
72 limitation of shock waves is that melting is generally investigated along the Hugoniot; this limitation can be
73 alleviated by sample pre-heating, pre-compression, ramp compression and thermodynamical modeling
74 (Asimow, 2018).

75 Concerning static experiments, reproducing the P-T conditions typical of deep mantle melting requires
76 today the use of the laser-heated diamond anvil cell (LH-DAC). LH-DAC has been used to determine
77 melting properties for a long time, initially for simple compounds (e.g. (Zerr and Boehler, 1993)) and later
78 for mantle relevant materials (Andrault et al., 2011; Fiquet et al., 2010; Nomura et al., 2014; Zerr et al.,
79 1998). Still, there are major discrepancies between the different works. They can have several origins:

80 (i) Mantle composition: Previous works report the melting properties of either peridotitic, pyrolitic or
81 chondritic-type mantle compositions. They differ in their (Mg,Fe,Ca)/Si ratio, which corresponds to variable
82 fractions of the major minerals of the lower mantle: (Mg,Fe)(Si,Al)O₃ Bg, CaSiO₃ perovskite (very recently
83 named davemaoite, Dvm) and (Mg,Fe)O ferropericlasite (Fp). More Fp is expected when going from pyrolite,
84 peridotite to harzburgite model compositions. Still, all these materials contain the same three phases and,
85 therefore, their melting behavior should not be very different. The solidus temperature, in particular, could be
86 very similar if eutectic-type melting prevails (Andrault et al., 2017; de Koker et al., 2013; Liebske and Frost,
87 2012). On the other hand, liquidus temperatures can be significantly different. The second aspect is the
88 content of minor and incompatible elements. The more the material is depleted, from chondritic-type to
89 pyrolite and peridotite, the purer the mineral phases (Bg, Fe and Dvm) must be (Corgne et al., 2005). This
90 can affect the melting properties of each mineral and, in return, modify slightly the mantle solidus. The
91 impact can be major when the mineral phases are saturated in a given incompatible element, which was
92 reported unlikely for typical mantle compositions (Irifune, 1994). Altogether, we are facing small changes of
93 composition. Slight changes of compositions between the materials relevant to the mean-mantle should have
94 a limited impact on the solidus, as long as the concentration of incompatible elements remains below the
95 limit of saturation of the mantle minerals (Irifune, 1994).

96 (ii) Melting criteria: several criteria have been used to detect the melting behavior: -change of optical
97 properties, -correlation between laser power and sample temperature, with possible appearance of a
98 temperature plateau and/or sudden temperature increase, -*in situ* monitoring of the phase content by X-ray
99 diffraction, -density contrasts using nano-tomography, -microstructure of recovered samples using electron
100 microscopy. Previous works generally use several of these criteria and report a good agreement between
101 them in a same study. When using the LH-DAC, the detection of solidus is facilitated by the fact that the
102 solid and liquid fractions absorb the laser radiation differently. The change of absorption coefficient of bulk
103 sample upon melting induces a change of heating behavior that is clearly detectable (Geballe and Jeanloz,
104 2012). Consequently, it is unlikely that controversies about the solidus temperature arise from the melting
105 criteria. The situation is much more complicated for the determination of the liquidus temperature, for which
106 a robust criterion should inform on the complete disappearance (melting) of all minerals within the hot
107 sample region, for a locally well-known chemical composition.

108 (iii) Experimental conditions: Beyond the definition of melting criteria, performing melting experiments
109 using the LH-DAC remains difficult in many aspects. We emphasize two parameters that can have a major
110 impact on determination of the solidus: water content and temperature measurements. Concerning the former,
111 approaching "dry" conditions requires specific procedures. For example, annealing a powder in a vacuum
112 oven is certainly insufficient to remove the water absorbed at the surface of sample grains. In addition, the

113 sample loading in air inevitably contaminates the sample with atmospheric water. Water can significantly
 114 lower the solidus, especially over the saturation limit of the mantle minerals. Concerning the latter;
 115 temperature measurements at very high temperature were shown to be more reliable when using reflective
 116 objectives, compared to refractive objectives (Giampaoli et al., 2018). In addition, refractive optics change
 117 their chromatic response when the optical path is slightly modified, which is common during LH-DAC
 118 experiments. The sample emissivity function should also be included in the temperature calculation.

119 In this work, we performed new measurements of the solidus temperature of several mantle materials,
 120 using *in house* optical, *in situ* X-ray diffraction and *post mortem* sample characterization techniques, in order
 121 to bring additional constraints on the melting behavior of the Earth's lower mantle.

122
123

124 Methods

125

126 Samples and DAC loading

127

128 We used a membrane-type DAC mounted with beveled diamonds and Re gaskets drilled using either
 129 spark erosion or laser ablation. Depending on the target pressure, we used beveled diamond anvils of
 130 250/300, 150/300, 100/300 or 75/300 μm internal/external diameters, gasket thicknesses from 45 μm to 15
 131 μm and hole diameters from 95 μm to 25 μm . One fresh piece of sample was used for each melting point
 132 determination. The nominal sample pressure was determined at 300 K from at least one of these methods:
 133 fluorescence of a ruby chip positioned in the pressure medium, Raman shift of the diamond anvil at the
 134 contact with the pressure medium (Suppl. Fig. 1), cell parameter of the KCl pressure medium determined
 135 using X-ray diffraction (Dewaele et al., 2012). Uncertainty in the determination of the nominal pressure at
 136 300K is a couple of GPa. Then, some thermal pressure develops in the sample at high temperature, due to
 137 partially isochoric heating in the LH-DAC. We apply a pressure correction (ΔP_{corr}) of half the theoretical
 138 thermal pressure (ΔP_{Th}), $\Delta P_{\text{corr}}=0.5\Delta P_{\text{Th}}=0.5(\alpha K_{\text{T}})_{\text{Bg}}(T_{\text{Exp}}-300)$ (Andraut et al., 2020), αK_{T} is the product of
 139 thermal expansion and isothermal bulk modulus of Bg (Fiquet et al., 2000), the most abundant phase in our
 140 samples, and T_{Exp} is the measured sample temperature. The final value of ΔP_{corr} is about $2.5 \cdot 10^{-3}$ GPa per
 141 Kelvin above 300 K, with an uncertainty $\pm 5\%$ at the melting temperature.

142 As starting materials, we used a natural enstatite and two
 143 synthetic glasses; pyrolite and MgSiO_3 . To probe the solidus of
 144 (Fe,Al)-bearing Bg, we selected a natural enstatite with low Fe and
 145 Al, namely $(\text{Mg}_{0.955},\text{Fe}_{0.045})(\text{Si}_{0.993},\text{Al}_{0.007})\text{O}_3$ (Table 1). The reason for
 146 this choice is an ambiguous solidus obtained in a previous study for a
 147 sample with high Fe and Al contents (Andraut et al., 2017), most
 148 probably because of incongruent melting and chemical migrations.
 149 The low Fe and Al contents in Bg are also relevant to melting
 150 conditions in the lower mantle, because of the relatively incompatible
 151 character of Fe and Al (Boujibar et al., 2016). On the other hand, the
 152 MgSiO_3 glass was synthesized in a classical furnace, while the glass
 153 of pyrolite (Table 1; (Ringwood, 1975)) was synthesized using the
 154 laser levitation technique. For the latter, the mixture of powders was
 155 carefully homogenized in an agate mortar and pre-compressed into a
 156 sphere. Levitation above a nozzle is performed by monitoring the flux
 157 of Ar with less than 0.05 ppm of oxygen, which yields a $\text{Fe}^{3+}/\Sigma\text{Fe}$
 158 ratio of 7-8 % in the silicate glass. Using infrared spectroscopy, the
 159 water content in the glass is found between 18 and 22 ppm, based on
 160 the Beer-Lambert law and absorption coefficients given for basaltic
 161 and basanitic glasses. A fragment of the starting material was loaded in the gasket hole between two layers of
 162 the KCl pressure medium. KCl is a material of first-choice to study the melting properties of silicates in the
 163 LH-DAC: -a very high melting temperature at high pressures, -no chemical reactions with silicates when it is
 164 dry, -good thermal insulation between hot-samples and cold-diamonds. The sample thickness was chosen to
 165 be $\sim 1/3$ of the gasket thickness, in order to limit the axial thermal gradients. These gradients are invisible to
 166 optical observations and yet the most critical ones in the LH-DAC.

167 We use special procedures to minimize the amount of water trapped in the pressure chamber: (i) all
 168 steps of the sample loading are performed inside a closed glove bag under a flux of dry air or N_2 . All the

Table 1: Composition of starting material determined using the electron microprobe.

	Opx	Opx	Pyrolite	Pyrolite
	JF15-67	JF15-67	Synth.	Synth.
	Wt%	Mole%	Wt%	Mole%
SiO ₂	59.32	50.63	46.53	40.51
TiO ₂	0.00	0.00	0.01	0.01
Al ₂ O ₃	0.33	0.17	4.55	2.34
Cr ₂ O ₃	0.40	0.13	0.01	0.00
FeO _t	3.10	2.21	8.57	6.24
MnO	0.06	0.00	0.02	0.01
MgO	36.47	46.40	37.55	48.74
CaO	0.35	0.32	2.11	1.97
Na ₂ O	0.16	0.13	0.03	0.02
K ₂ O	0.02	0.00	0.28	0.15
Total	100.22	99.99	99.66	100.00
Fe/(Mg+Fe)		0.045		0.113
Al/Fe		0.154		0.750
Al/(Al+Si)		0.007		0.104

169 necessary material is dry and inserted in advance in the bag where a numerical water sensor is permanently
170 operational. (ii) Coarse grains of KCl are kept in oven at 130-150 K all the time. (iii) The starting material
171 and a KCl grain are crushed inside the glove bag. We do not crush the sample in fine powder that inevitably
172 adsorb water. Instead, we load a shard of convenient size and shape in the gasket hole. Several criteria are
173 typical of a dry system, like no adhesion between the loaded materials and a needle, except for a weak
174 electrostatic bonding. Presence of humidity can also be detected optically at the surface of the diamond culet.
175 Then, when we would measure a melting temperature lower compared to previous measurements, we reload
176 the cell with new sample and loading tools, to check the melting temperature in another experiment.

177 178 Optical set-up, laser heating and temperature measurements

179
180 We used two optical set-ups (i) for melting MgSiO₃ at ID27 and (ii) for all other experiments in LMV.
181 Both systems follow the basic principles established several years ago (Schultz et al., 2005): in particular,
182 they are both equipped with reflective optics. It was shown that they are superior to refractive optics for
183 determination of very high temperatures in the LH-DAC (Giampaoli et al., 2018). The new laser heating
184 system of LMV (Suppl. Fig. 2) is optimized for simultaneous temperature measurements on both sample
185 sides (using the TRax software (Holtgrewe et al., 2019)). On ID27, temperature was measured on both
186 sample sides prior to performing angle-dispersive X-ray diffraction with monitoring of temperature on one
187 sample side only. The MgSiO₃ sample was first heated using a CO₂-laser (10μm radiation) until
188 crystallization of small grains of Bg made the sample slightly opaque to visible light. Then, two fiber lasers
189 (IPG fiber photonic lasers YLR-100-AC producing 1.03μm radiation) could heat the sample up to the
190 melting point. Similarly, fiber lasers were used to study the melting behavior of (Fe,Al)-bearing Bg and
191 pyrolite. The two lasers arrive with an angle of incidence of about 15° with respect to the cell axis and are
192 focused on the sample using silica lenses with a focal length of 75 mm, or 50 mm when the pressure exceeds
193 ~80 GPa. The laser paths are remotely controlled using piezoelectric actuators.

194 Temperatures up to 5200 K were measured from the sample thermal emission in the visible range
195 (600 to 1000 nm; Suppl. Figs. 3-5). We dedicated a special care to cross-calibrate the optical response of
196 ID27 and LMV optical systems. For this, we used (i) a platinum heating wire calibrated on the melting points
197 of wollastonite (1817 K) and diopside (1664 K), (ii) a newly acquired commercial lamp calibrated on a
198 formal black body and (iii) an additional tungsten lamp calibrated at LMV and measured at ID27, and vice
199 versa. In addition, we reworked the general assumptions made on the sample emissivity function ($\epsilon(\lambda)$),
200 which most commonly are (i) a grey-body sample (constant $\epsilon(\lambda)$) or (ii) same $\epsilon(\lambda)$ for the sample and the W-
201 lamp. We found that the second one is more in agreement with the data available for $\epsilon(\lambda)$ of silicates (see
202 (Andraut et al., 2022)). For a sample showing a wavelength-dependent (WD) emissivity, using the black
203 body (BB) assumption yields temperature (T_{BB}) overestimated by ~65, ~151, ~280 and ~464 K for a true
204 sample temperature (T_{WD}) of 2000, 3000, 4000 and 5000 K, respectively; the 2nd-order polyhedral relation
205 between T_{BB} and T_{WD} is: $T_{BB}-T_{WD}=2.585 \cdot 10^{-5} \cdot T_{WD}^2 - 4.814 \cdot 10^{-2} \cdot T_{WD} + 60.46$. A further argument in favor of
206 wavelength-dependent $\epsilon(\lambda)$ for silicates is the solidii of SiO₂ (Andraut et al., 2022) and MgSiO₃ (see Result
207 section below) falling in very good agreement with shock wave experiments (Akins and Ahrens, 2002) and
208 ab initio calculations (e.g. (Usui and Tsuchiya, 2010)). Following this observation, we will propose a
209 temperature correction to the previous reports of the solidii of peridotite (Fiquet et al., 2010) and chondritic-
210 type mantle (Andraut et al., 2011).

211 Another major source of uncertainty comes from temperature gradients: Both optical systems used in
212 this study analyze the thermal emission signal coming from a sample region of 2-3 microns diameter at the
213 center of the laser spot, which minimizes the effect of radial temperature gradient. On the contrary, axial
214 temperature gradients produce superimposition of thermal radiation spectra coming from sample regions at
215 different temperatures, when probing an optically transparent sample. Still, the distortion could remain minor
216 because the hottest region of the sample (i.e. where melting occurs first) provides the strongest contribution
217 to thermal emission.

218 We note that the sample microstructure becomes heterogeneous after melting, due to melt migration. It
219 affects the laser-absorption as well as the thermal emissivity function, potentially; It can yield distortion of
220 the thermal emission spectrum. For this reason, we always use a fresh piece of sample for each determination
221 of the melting temperature.

222 Finally, we noticed a higher temperature uncertainty when using the lasers at high power (when
223 approaching 100 watts). Reasons for this can be (i) stronger axial temperature gradients in the DAC, yielding
224 less stable temperature at the center of the sample, (ii) convection of air between the diamond cell and the
225 schwarzchild objectives, inducing optical fluctuation, (iii) difficulties to detect the temperature vs laser-

226 power plateau. For this reason, we favor loadings with thick layers of insulating KCl on both sides of a thin
227 sample. Taking all possible precautions, the uncertainty of a given temperature measurement at the highest
228 temperatures is ~50 K (Suppl. Fig. 3).

229

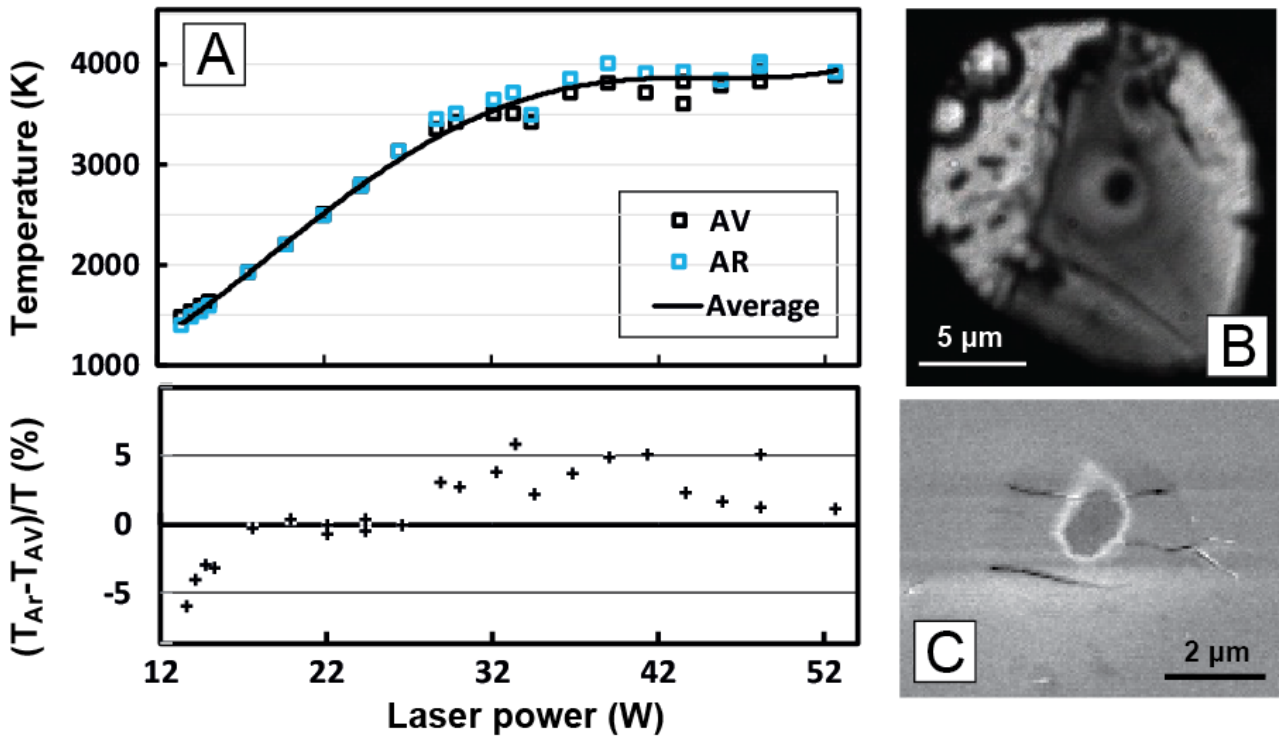
230 Melting criteria

231

232 To investigate melting of pure MgSiO₃-Bg, we monitored the change of structural properties using X-
233 ray diffraction at the ID27 beamline, using the same procedure as in our recent work on SiO₂ (Andrault et al.,
234 2020). With increasing temperature, the diffraction rings progressively evolve from coarse and rounded for
235 the compressed glass, continuous and very fine for nano-crystalline Bg, spotty after severe grain growth of
236 Bg grains and, finally, a few diffraction spots, which change positions very fast with time when the sample
237 gets molten. X-ray diffuse scattering of the melt also appears at the melting point (Andrault et al., 2020;
238 Fiquet et al., 2010); However, we do not use amplitude of X-ray diffuse scattering and full disappearance of
239 all diffraction peaks as major criteria. The reason is the axial temperature gradient between the two diamonds,
240 which inevitably induce crystallization close to cold diamonds, while the melting temperature is already
241 reached at the center of the sample.

242 For Fe-bearing samples, crystallization was detected by changes in the absorption properties. Next, we
243 performed incremental steps of 0.2 to 0.4 watts during careful monitoring of the temperature, with a special
244 care to detect any anomaly in the sample behavior. An entire experiment generally takes ~30 minutes with a
245 time interval of 30 to 60 seconds between two temperatures. At a sample pressure of e.g. 138 GPa, three
246 distinct sample behaviors can be distinguished (Fig. 1a, see also Suppl. Figs. 4 and 5): (i) a regular increase
247 of temperature for laser power between 12 and 32 watts. (ii) a plateau with no significant increase of
248 temperature for laser power between 32 to 52 watts. On the plateau, temperature fluctuations are less than
249 5%. This plateau is interpreted as a progressive increase of the melt fraction in the sample with laser power,
250 with a melt absorbing less the laser radiation than the solid part. This can happen for (Fe,Al)-Bg that contains
251 both Fe²⁺ and Fe³⁺ in large amounts, which implies good absorption of the 1 μm laser radiation. Less Bg
252 implies a higher laser power for maintaining a similar sample temperature. This behavior was well
253 established based on the combination of several other melting criteria and modeling of the sample behavior
254 (Andrault et al., 2014; Geballe and Jeanloz, 2012; Thomson et al., 2014). (iii) a larger fluctuation of the
255 sample temperature with further increase of the laser power, before a jump to temperatures 1000 to 2000 K
256 higher than the temperature plateau. This arises when the laser power becomes sufficient to heat the melt
257 above the solidus. Another possible explanation is a low thermal conductivity of the melt, which would
258 induce a higher sample temperature in the sample center (Shen and Lazor, 1995). Altogether, the solidus
259 temperature and its uncertainty, between 50 to 150 K, are determined after averaging the highest
260 temperatures measured on the plateau.

261 After laser shutdown, the sample microstructure provides another criterion for occurrence of melting
262 (Fig. 1b). In particular, the presence of a dark blob at the center of the laser spot is a good indicator of melt
263 migration. The blob is often surrounded by a lighter shell of material, likely Bg depleted in Fe (Nabiei et al.,
264 2021). We further characterized the microstructure of selected samples using high-resolution scanning
265 electron microscope (SEM) at CIMAP, following previous works of the same kind (Fiquet et al., 2010;
266 Nomura et al., 2011; Tateno et al., 2014). For this, we prepared thin sections using the focused Ga-ion beam
267 FIB. Cuts were performed perpendicularly to the sample surface across the laser-heated area, which yields an
268 observable sample surface along the paths of the infrared lasers between the two diamonds. Melting induces
269 solid-melt segregation, with a higher Fe-concentration in the melt easily detectable in the SEM (Fig. 1c,
270 (Nabiei et al., 2021)). We note that the microstructure of the molten regions can be complex due to fast
271 recrystallization upon quenching.



273 **Figure 1: Melting criteria for LMV experiments:** (a) Temperature as a function of increasing laser power
 274 for a sample of pyrolite loaded at 138 GPa, yielding a solidus melting temperature of 3950(200) K. "Av" and
 275 "Ar" temperatures are measured on each side of the sample. On bottom left, we report the temperature
 276 difference between the two sides of the sample (b) Optical microphotograph showing a black spot at the
 277 center of the sample after melting at 94 GPa. (c) SEM microphotograph (secondary electrons) of the melted
 278 region at 65 GPa. There is central blob of melt enriched in Fe (darker zone; as in (Nabiei, 2017)), surrounded
 279 by a first shell of Fe-depleted bridgmanite (lighter zone) and the un-molten pyrolite sample further from the
 280 sample. Other examples of the experimental determination of solidii are reported in [Suppl. Figs. 4 and 5](#).

281

282

283 Results

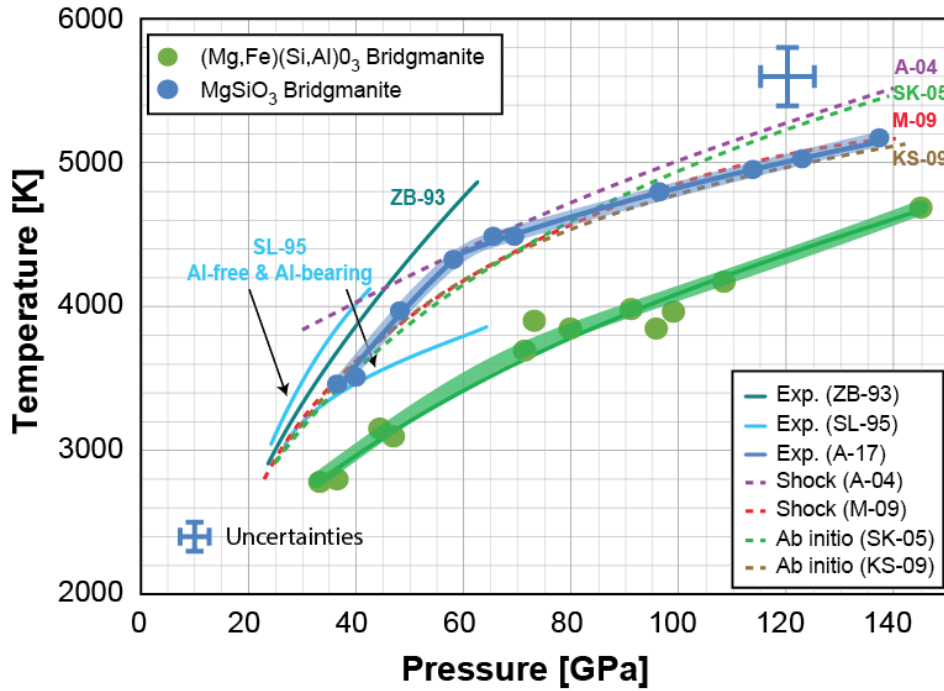
284

285 Solidus of MgSiO₃ bridgmanite

286

287 The solidus of MgSiO₃ was determined from 10 different measurements performed at pressures between
 288 35 GPa and 3400K, and 140 GPa and 5200 K ([Fig. 2, Table 2](#)). The data plot within the range of melting
 289 temperature proposed in previous studies. Up to ~60 GPa, the slope of our solidus is comparable with
 290 previous LH-DAC measurements on Al-free Bg (Shen and Lazor, 1995; Zerr and Bohler, 1993), even
 291 though our melting temperature plots 200-300 K lower. This corresponds to a steep Clapeyron slope of ~42
 292 K/GPa between ~25 and 60 GPa. At high mantle pressures, our MgSiO₃-Bg solidus is in good agreement
 293 with previous *ab initio* calculations (de Koker and Stixrude, 2009) and shock wave experiments
 294 (Mosenfelder et al., 2009). Between 60 and 140 GPa, the Clapeyron slope becomes ~10 K/GPa. Due to the
 295 change of slope, we modeled the solidus using two different modified Simon and Glatzel equations
 296 [$T=T_0(P/a+1)^{1/c}$] (Simon and Glatzel, 1929): $T_0=274$ K, $a=0.2644$ GPa and $c=1.9575$ between 35 and 60
 297 GPa, and $T_0=403$ K, $a=0.00028$ GPa and $c=5.1377$ between 60 and 140 GPa ([Table 3](#)). We note that while
 298 the (T_0 , a , b) parameters constrain the melting temperature at a given pressure, the slope and the curvature of
 299 the melting curve, each parameter has no formal significance when taken independently of the other two,
 300 especially for melting curves restricted to high pressure regions.

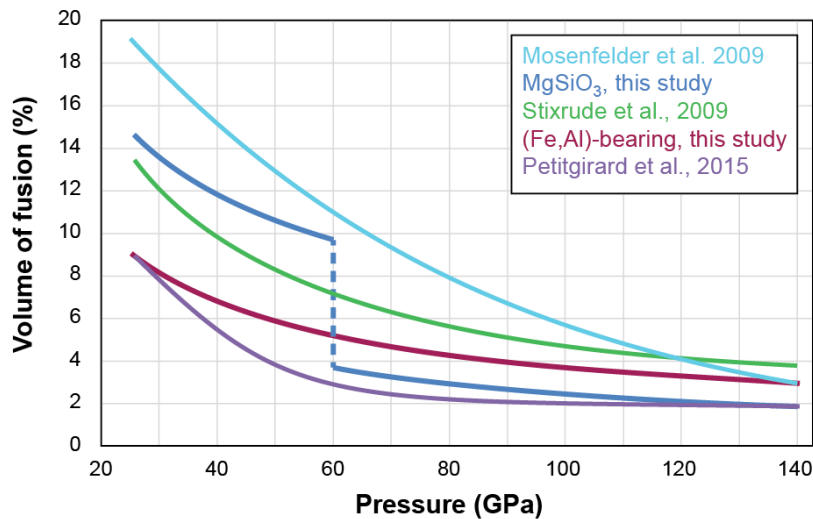
301 This change of behavior around 60 GPa denotes a marked change in the thermodynamic parameters,
 302 most probably a decrease of the volume of fusion (ΔV_m), or a decrease in entropy of fusion, with increasing
 303 pressure. Such effect could be due to higher compression rate of the melt, compared to Bg. A major
 304 ingredient of melt compaction is the change of Si coordination number from 4 to 6. Our MgSiO_3 solidus
 305 suggests a relatively abrupt Si coordination change in the melt at ~ 60 GPa. Using the Clapeyron relation
 306 ($dT/dP = \Delta V_m / \Delta S_m$) and an entropy change upon melting (ΔS_m) of 63.7 J/molK (Stixrude et al., 2009), we
 307 estimate the volume of fusion for MgSiO_3 . Based on the Simon and Glatzel equations, we obtain $\Delta V_m / V_{Bg}$
 308 (with V_{Bg} the molar volume of Bg) decreasing from 15% to 2% with increasing pressure from 25 to 135 GPa,
 309 respectively (Fig. 3). The abruptness of the ΔV_m change at ~ 60 GPa is overestimated due to the use of
 310 different equations above and below the transition pressure.



311 **Figure 2: Solidus of bridgmanite:** We report our work on MgSiO_3 (blue dots) and
 312 $(\text{Mg}_{0.955}, \text{Fe}_{0.045})(\text{Si}_{0.993}, \text{Al}_{0.007})\text{O}_3$ (green dots) bridgmanite together with previous studies: LH-DAC on
 313 $(\text{Mg}_{0.88}\text{Fe}_{0.12}\text{SiO}_3)$ (ZB-93, (Zerr and Bohler, 1993)), MgSiO_3 and $\text{Mg}_3\text{Al}_2\text{Si}_3\text{O}_{12}$ (SL-95; (Shen and Lazor,
 314 1995)), shock waves on MgSiO_3 (A-04; (Akins et al., 2004), M-09; (Mosenfelder et al., 2009)) and *ab*
 315 *initio* calculations for MgSiO_3 (KS; (de Koker and Stixrude, 2009), SK-05; (Stixrude and Karki, 2005)).
 316

317
 318 Solidus of $(\text{Mg}_{0.955}, \text{Fe}_{0.045})(\text{Si}_{0.993}, \text{Al}_{0.007})\text{O}_3$ bridgmanite
 319

320 Twelve different measurements have been performed to determine the solidus of our (Fe,Al)-bearing Bg
 321 compound. We note that this (Fe,Al)-bearing compound may not melt congruently at the solidus, however,
 322 our experimental method cannot resolve the finite melting interval between the solidus and the liquidus. The
 323 solidus is found between 500 and 1000 K lower than that of MgSiO_3 , even though this enstatite sample
 324 presents relatively low Fe and Al contents, compared to mantle composition. Still, the several minor
 325 elements present in this natural phase (Table 1) may also play a role in reducing the melting temperature.
 326 The solidus appears more linear in the pressure range investigated, compared to MgSiO_3 , which points out a
 327 more progressive melt compaction. We acknowledge that our data set presents some scattering between 70
 328 and 100 GPa, which may be related to chemical heterogeneities in the starting material. For this reason, we
 329 reproduced the measurements several times. Nevertheless, the maximum temperature difference remains
 330 within a reasonable range of uncertainties of 200-300 K. The entire solidus can be satisfactorily fitted using a
 331 single Simon and Glatzel equation with $T_0 = 241$ K, $a = 0.03145$ GPa and $c = 2.8501$ (Table 3). Its Clapeyron
 332 slope evolves from ~ 28 to ~ 12 K/GPa in the pressure range investigated. Finally, we calculate ΔV_m based on
 333 the same value of ΔS_m as for MgSiO_3 . As expected from the difference in the solidii, ΔV_m decreases more
 334 progressively with increasing the pressure, compared to MgSiO_3 (Fig. 3).



335

336

337

338

339

340

341

342

343

344

345

346

347

348

349

350

351

352

353

354

355

356

357

358

359

360

361

362

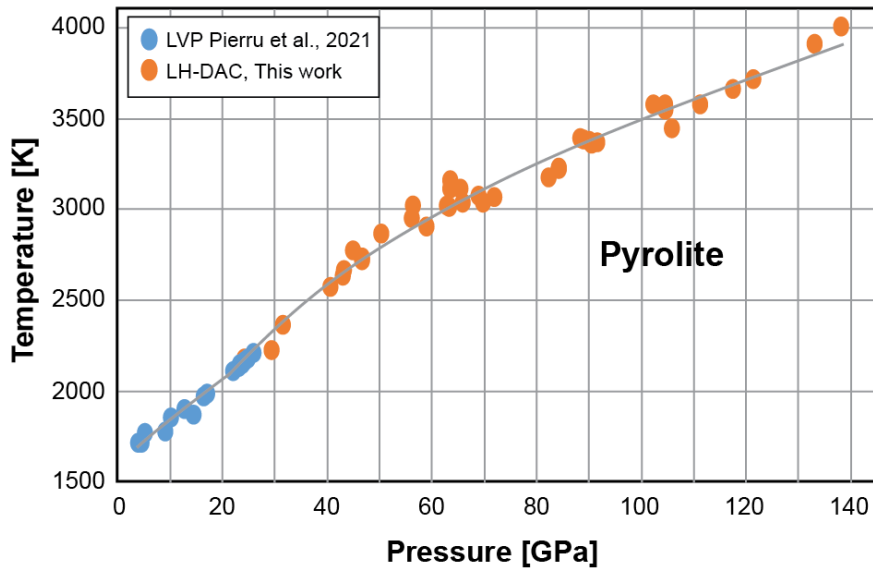
363

Figure 3: Volume of fusion ($\Delta V_m/V_{Bg}$) for bridgmanite. We report our data for $MgSiO_3$ and $(Mg_{0.955}, Fe_{0.045})(Si_{0.993}, Al_{0.007})O_3$ bridgmanite phases and $MgSiO_3$ $\Delta V_m/V_{Bg}$ obtained based on shock-wave experiments (Mosenfelder et al., 2009), ab initio calculations (Stixrude et al., 2009) and glass density measurements (Petitgirard et al., 2015). For $MgSiO_3$ data, our calculation overestimates the sharpness of the transition at ~60 GPa.

Solidus of dry pyrolite

We performed 39 determination of the melting for our pyrolite glass (Table 2). In the lower mantle, pyrolite yields a mineral assemblage made of Bg, Dvm and Fp. As a result, progressive sample melting is expected between the solidus and liquidus temperatures. In this study, we dedicated our experimental efforts to the determination of the solidus profile (Fig 4). It exhibits a smooth evolution from 2200(100) K to 3950(200) K for pressures between 24 GPa (the 660 km depth discontinuity) to 140 GPa (close to CMB), respectively. The solidus presents a significant curvature, which corresponds to a Clapeyron slope evolving from 28 to 13 K/GPa in the pressure range investigated, which is very similar to the values obtained for our (Fe,Al)-Bg compound. Still, the solidus of pyrolite plots 500-600 K lower. In addition to 3 phases, instead of one for (Fe,Al)-bearing Bg, pyrolite contains a significantly larger amount of incompatible elements, which can also contribute to lowering the solidus.

In the low pressure range, our solidus plots in very good agreement with our recent determination of the solidus at pressures up to 27 GPa, using the multi-anvil apparatus (Pierru et al., 2022). We note that higher melting temperatures were proposed for the melting of mantle-relevant materials in the upper mantle and transition zone (e.g. (Litasov and Ohtani, 2002; Tronnes and Frost, 2002)). The discrepancy may arise from several factors, including a rather high melt fraction reported in previous work. This matter is discussed at length elsewhere (Andrault et al., 2018; Pierru et al., 2022). To provide a convenient model for the pyrolite solidus at all mantle pressures, we coupled the two data sets on the same pyrolitic sample and fitted two Simon and Glatzel equations (Fig. 4). We obtain $T_0=1609$ K, $a=61.1176$ GPa and $c=1.1288$ for the pressure range between 5 and 24 GPa and $T_0=235$ K, $a=0.0300$ GPa and $c=3.0067$ between 24 and 138 GPa (Table 3).



364 **Figure 4: Solidus of pyrolite:** Data sets from multi-anvil press ((Pierru et al., 2022), blue dots) and diamond
 365 anvil cell from this work (orange dots) are combined to determine the solidus of pyrolite at all mantle-
 366 relevant pressures.
 367

368
 369
 370
 371
 372
 373
 374 **Table 2: Experimental data:** Summary of
 375 all experimental measurements of solidii
 376 reported in this work
 377

MgSiO ₃		(Fe,Al)-bearing Bg		Pyrolite		(continued)	
P(GPa)	T(K)	P(GPa)	T(K)	P(GPa)	T(K)		
58.1	4321	33.2	2780	24.1	2184	69.0	3080
65.5	4479	36.5	2800	29.4	2230	69.8	3039
96.2	4790	33.2	2780	31.5	2364	71.9	3072
113.6	4942	36.5	2800	40.6	2579	82.2	3175
122.8	5018	45.1	3152	43.0	2638	84.3	3225
137.2	5167	47.0	3100	43.1	2670	84.3	3230
40.0	3504	71.5	3700	45.0	2775	88.3	3385
69.5	4479	73.4	3900	46.7	2721	88.9	3378
36.4	3462	79.9	3850	46.7	2738	90.1	3373
48.2	3959	91.2	3986	50.4	2867	90.4	3357
		95.9	3850	56.1	2955	91.7	3366
		99.2	3966	56.3	3021	102.2	3579
		108.7	4171	59.0	2906	104.6	3530
		145.0	4691	62.8	3023	104.7	3565
				63.2	3016	105.9	3450
				63.4	3118	111.2	3575
				63.6	3163	117.4	3664
				65.4	3116	121.5	3715
				65.9	3041	133.0	3900
						138.3	4000

377
 378
 379
 380
 381
 382
 383
 384
 385
 386
 387 **Table 3: Melting equations:** Summary of the parameters
 388 refined for Simon&Glatzel melting equations through
 389 data points of MgSiO₃ and our (Fe,Al)-bearing Bg, and
 390 pyrolite.
 391
 392

Simon et Glatzel equations			
Compound	MgSiO ₃	(Fe,Al)-Bg	Pyrolite
P-range (GPa)	35-60	32-145	5-24.
T0 (K)	274	241	1609
a (GPa)	0.2644	0.03145	61.118
c	1.9575	2.8501	1.1288
P-range (GPa)	60-140		24-138
T0 (K)	403		235
a (GPa)	0.00028		0.0300
c	5.1377		3.0067

393 **Discussion**

394

395 Mantle solidus: Comparison between different studies

396

397

398

399

400

401

402

403

404

405

406

407

408

409

410

411

412

413

414

415

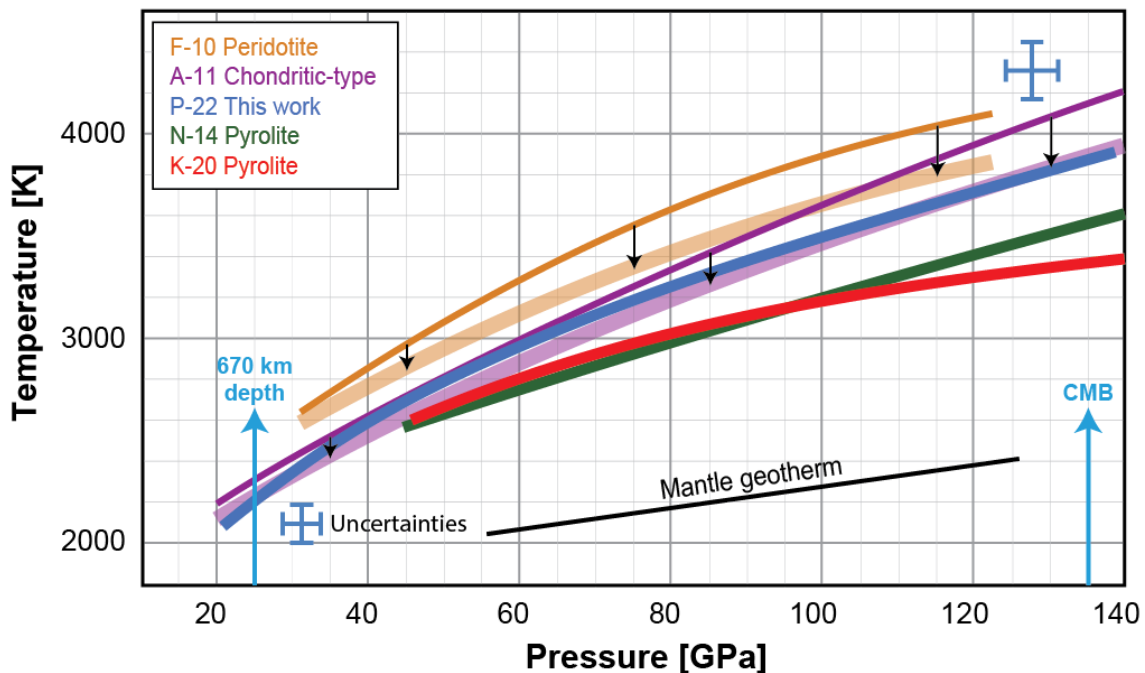
416

417

418

419

We compare our pyrolite solidus with other recent determinations of the solidus for various mantle relevant compositions (Fig. 5). We make the following observations: (i) Our solidus plots 300-400 K lower than that reported for peridotite (F-10; (Fiquet et al., 2010)). (ii) It is very compatible with many studies between 20 and 50 GPa; however the different studies diverge at higher mantle pressures to become (iii) 100-150 K lower than that reported for chondritic-type mantle (A-11; (Andraut et al., 2011)) and (iv) 300-500 K higher than other reports for pyrolite by (N-14; (Nomura et al., 2014)) and (K-20; (Kim et al., 2020)) at the CMB conditions. At this point, we note that F-10, A-11 and our new study were performed in very similar conditions, in particular with same type of synthetic starting material and similar optical systems mounted with reflective objectives. A major difference, however, is how the sample emissivity $\epsilon(\lambda)$ was considered to calculate temperatures from thermal emission. F-10 and A-11 assume a grey-body function (i.e. $\epsilon(\lambda)=\text{constant}$), while this method could induce artifacts (Deng et al., 2017). Unfortunately, $\epsilon(\lambda)$ is not known for silicates at the high P-T investigated in this study. So far, the most appropriated assumption could be same $\epsilon(\lambda)$ as the W-lamp (see (Andraut et al., 2022)). We calculate a temperature correction, of a couple 100 K, that would account for wavelength-dependent thermal emission of peridotite and chondritic-type mantle in previous studies (light orange and purple bands in Fig. 5). For A-11, we also include in the calculation the solidus data points reported for the same sample based on multi-anvil press work (Andraut et al., 2018). Interestingly, the corrected chondritic-type solidus falls in perfect agreement with our pyrolite solidus. This result is coherent with the small difference between these two compositions, which have a similar fertility (amount of minor incompatible elements) and for which the main differences are the Bg, Dvm and Fp phase fractions. Concerning F-10 data, the corrected values plot 200-300 K above ours, which could be due to a more depleted peridotite composition. The three data sets (F-10, A-11 and our pyrolite data) converge to a solidus temperature of 3950(200) K at the 135 GPa of the CMB.



420

421

422

423

424

425

426

427

428

Figure 5: Solidus temperatures of various mantle materials. We plot the new pyrolite solidus (P-22) together with previous reports (F-10, (Fiquet et al., 2010); A-11, (Andraut et al., 2011); N-14, (Nomura et al., 2014); K-20, (Kim et al., 2020)). For F-10 and A-11, we report both the original solidii (thin orange and purple lines) and the corrected solidii (light but thicker lines indicated by black arrows) for which temperatures have been recalculated taking into account the wavelength-dependent thermal emission (see text).

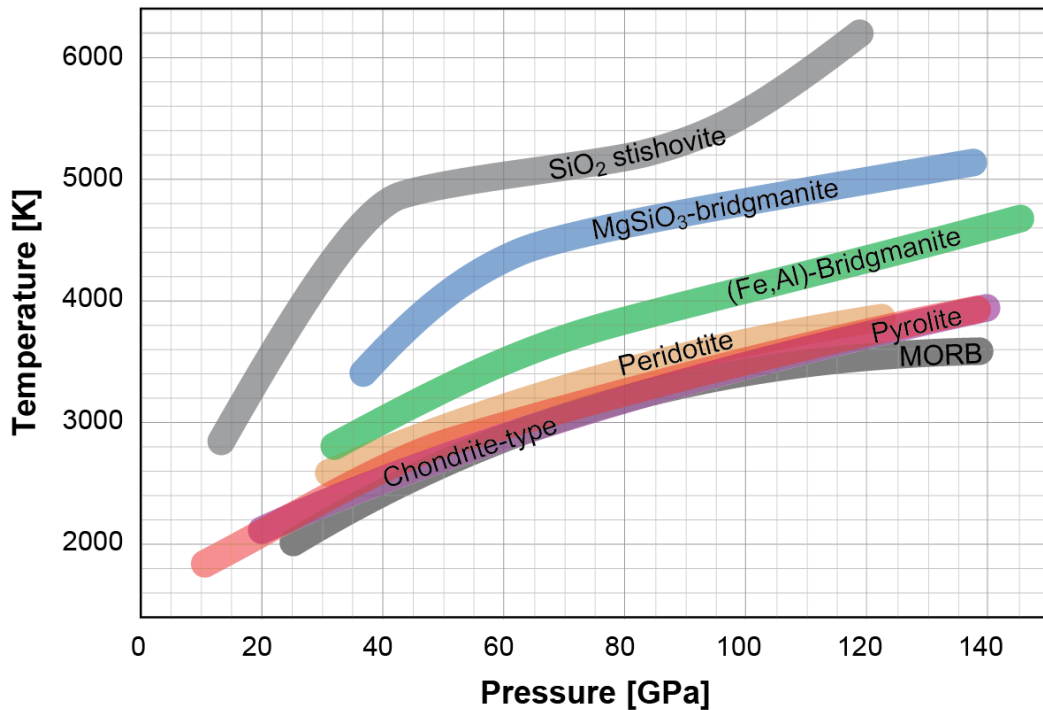
The N-14 and K-20 data sets that plot significantly lower than ours, for which the most likely explanation is the presence of some water in these experiments. Noticeably, the K-20 data set plots at lower

429 temperatures than N-14, for which the reported water content in the sample is 400 ppm. In K-20 work,
 430 vacuum oven was used to dry powders before loading and then to dry the entire DAC after loading. In our
 431 previous experience on melting of chondritic-type mantle (Andraut et al., 2011), we did not succeeded to
 432 reproduce the solidus using starting materials made of powders, and always found much lower temperatures.
 433 Our explanation is that annealing temperatures much higher than e.g. 150°C (i.e. oven) are needed to remove
 434 the water adsorbed at the surface of the grains. Fine powders can adsorb a significant amount of water in a
 435 few minutes. For this reason, we use chips of glass for the loading in the DAC and all loadings are performed
 436 in a glove bag flushed with inert atmosphere.

437
 438 Comparison of the curvatures of solidii

439
 440 We plot together the solidii of various silicate phases. To strengthen the comparison, we selected the
 441 works performed using the same methodology (Fig. 6); in addition to compositions discussed above, we
 442 include SiO₂ (see (Andraut et al., 2020) and its "comment" taking into account its wavelength-dependent
 443 behavior (Andraut et al., 2022)) and mid-ocean ridge basalt (MORB; (Andraut et al., 2014), also corrected
 444 here for its $\epsilon(\lambda)$). As logically expected, the larger the amount of cations entering in the sample composition
 445 [N_{Cat}], from 1 to 6 between pure SiO₂ and our pyrolite sample, the lower is the solidus. Another interesting
 446 observation is the curvature of the melting slope, which (i) is significantly less pronounced and (ii) appears at
 447 higher pressure, with increasing N_{Cat}. A sharp change of the Clapeyron slope is found around 40 GPa for
 448 SiO₂, it is also clear at 60 GPa for MgSiO₃, one could argue for a deviation in the 60-80 GPa range for
 449 (Mg_{0.955},Fe_{0.045})(Si_{0.993},Al_{0.007})O₃ Bg, and the solidi present a progressive change between ~40 and ~100 GPa
 450 for mantle-relevant peridotitic, chondritic-type, or pyrolitic compositions. Since this curvature denotes a
 451 change of the volume of fusion with increasing pressure, the observed trend is consistent with a more abrupt
 452 change in the cation coordination number when N_{Cat} is smaller. The major structural change at mantle depth
 453 being the Si coordination change from 4 to 6, it suggests that the coexistence in the melt of the two structural
 454 entities, SiO₄ and SiO₆, is facilitated for a larger number of cations. Interestingly, the MORB solidus is
 455 significantly more curved than the mean-mantle relevant compositions. This effect could arise from a higher
 456 SiO₂ content in this material.

457



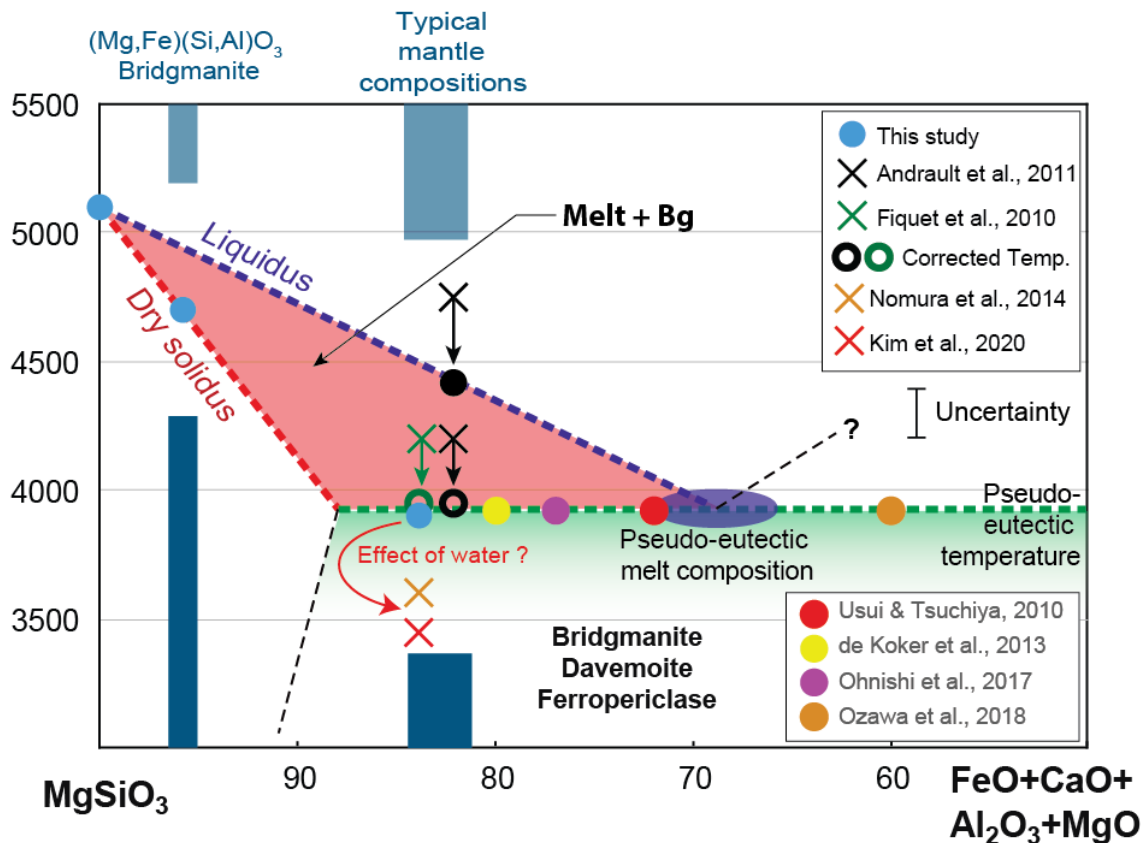
458 **Figure 6: Solidii of various silicates.** To improve the strength of the comparison, we only report the solidii
 459 of silicate phases determined using the same experimental techniques, in particular (i) reflective objectives
 460 that offer a best temperature measurement at high temperature (Giampaoli et al., 2018) and (ii) dry glasses
 461 loaded using a glove bag flowed by inert atmosphere. SiO₂ (Andraut et al., 2020; Andraut et al., 2022),
 462 peridotite (Fiquet et al., 2000), chondritic-type mantle (Andraut et al., 2011), MORB (Andraut et al., 2014)
 463 and MgSiO₃, (Mg_{0.955},Fe_{0.045})(Si_{0.993},Al_{0.007})O₃, and pyrolite (this work).

464
465
466
467
468
469
470
471
472
473
474
475
476
477
478
479
480
481
482
483
484
485
486
487
488
489

Building the melting diagram at mantle depth: example of the core-mantle boundary

Several approaches have been developed to discuss the thermodynamics of mantle melting in the lower mantle. One of them consists in refining the thermodynamical properties of silicate melts with end-member compositions, such as MgSiO_3 , MgO , SiO_2 , etc., using either first-principles molecular dynamics simulations or shock-wave experiments (Asimow, 2018; de Koker et al., 2013; Mosenfelder et al., 2009; Stixrude et al., 2009; Stixrude and Karki, 2005). Then, melting properties of mantle-relevant compositions can be modeled based on well-defined mixing properties between the end-members. In this work, we provide directly the solidii, which unfortunately does not help to constrain the basic thermodynamic parameters, but which can help constraining the melting diagrams.

If we leave to further works the goal to solve the controversy about the solidus of pyrolite, there is an overall good coherence on the solidii of the different silicate compositions (Fig. 6). If we focus on the CMB, data sets (F-10, A-11 and this work) converge to a solidus mantle temperature of 3950(200) K (Fig. 5). In these conditions, the melt composition is not well constrained and it anyway depends on the degree of partial melting. Nevertheless, previous studies performed at less extreme pressures suggest a pseudo-eutectic melt composition close to peridotite, based on multi-anvil press (Ito et al., 2004) and LH-DAC experiments (e.g. (Tateno et al., 2014)). Based on this, we draw a pseudo-binary phase diagram between MgSiO_3 -Bg and a mixture of the other oxides (Fig. 7; see details of the strategy in (Andrault et al., 2017)). We model a linear solidus profile from the melting temperature of MgSiO_3 -Bg and our (Fe,Al)-bearing Bg. Similarly, a linear liquidus profile is drawn from melting point of MgSiO_3 -Bg to the liquidus temperature of the chondritic-type mantle (Andrault et al., 2011). The linear extrapolation of the liquidus to a pseudo-eutectic temperature of 3950 K yields an estimated composition of the pseudo-eutectic melt. Here, we do not consider the liquidus temperature of ~5400 K proposed for peridotite at the CMB (Fiquet et al., 2010), because such experimental temperature corresponds more likely to the melting temperature of pure Bg.



490 **Figure 7: Melting diagram of silicate mantle at the CMB pressure of 135 GPa:** A pseudo binary diagram is presented in which one pole is MgSiO_3 bridgmanite and a second one regroups all other elements (FeO, CaO, Al_2O_3 and MgO). The left blue vertical line corresponds to the composition of bridgmanite investigated in this study. The second vertical line corresponds to typical mantle compositions. We compare our estimate of the melt composition at the pseudo-eutectic temperature (purple ellipse) with previous reports in the MgO - MgSiO_3 system (de Koker et al., 2013; Ohnishi et al., 2017; Ozawa et al., 2018; Usui and Tsuchiya, 2010).

496
497
498
499
500
501
502
503
504
505
506
507
508
509
510
511
512
513
514
515
516
517
518
519
520
521
522
523
524
525
526
527
528
529
530
531
532
533
534
535
536
537
538
539
540
541
542
543
544
545

The melting diagram (Fig. 7) yields important information: -the higher the Bg content, the closer the solidus temperature is to that of the MgSiO₃-Bg end-member. -The Bg grains in equilibrium with mantle melts should be significantly enriched in Fe and Al with decreasing temperature below the liquidus. -The pseudo-eutectic melt composition at the CMB should be significantly depleted in SiO₂ (i.e. enriched in FeO, CaO, MgO and/or Al₂O₃), compared to classical models of mean mantle composition. Our estimated value plots within the interval of values reported for the simplified MgO-MgSiO₃ composition at the CMB (de Koker et al., 2013; Ohnishi et al., 2017; Ozawa et al., 2018; Usui and Tsuchiya, 2010) -Finally, the difference between solidus and liquidus reaches a maximum of ~700 K for a mantle composition with ~90% of MgSiO₃ and it decreases progressively with increasing the Fp and Dvm contents up to the pseudo-eutectic composition (where solidus and liquidus temperatures are equal).

Thermal state of the core-mantle boundary

Extrapolation of the mantle geotherm along an adiabatic gradient to the 135 GPa yields a value of ~2630 K(60) at the CMB, based on the elastic parameters of the mantle constituent minerals (Katsura et al., 2010). This does not take into account a possible super-adiabatic temperature gradient in the lower mantle. By performing global inversion of seismic radial profiles based on compressional and shear properties of the minerals, the lowermost mantle temperature was refined between 2800 and 3400 K (Matas et al., 2007). Such type of modeling is poorly sensitive to the rapid change of temperature occurring in the thermal boundary layer extending a few 100 km above the CMB. It was proposed that the Bg to post-Bg transition, which is sharp for MgSiO₃ composition, provides a constraint for the temperature in this region (Hernlund, 2010). Supposing that the loop-shaped low-velocity regions of the lowermost mantle correspond to a double crossing between the mantle temperature profile and the Clapeyron slope of this transition, the CMB temperature is estimated at ~3700 K (Tateno et al., 2009). Unfortunately, the Bg to post-Bg transition is progressive and occurs at too high pressures for a relevant (Fe,Al)-bearing mantle compositions (Andraut et al., 2010; Catalli et al., 2009), which shed doubts on this method. From core properties, the CMB temperature is estimated to ~4050 K, based on the melting point of a relevant Fe-alloy at the inner-core boundary (Anzellini et al., 2013).

A CMB temperature of 4050 K would be similar or higher than the mantle solidus, which we refine at 3950(200) K for 135 GPa in this study (Fig. 5). It would induce global mantle melting at the contact of the core, which is incompatible with seismic observations of ULVZ (e.g. (Yu and Garnero, 2018)). Instead, the CMB temperature should be lower than ~3950 K. Uncertainties remain regarding the fertility of the mantle located above the CMB, which could range from undepleted primitive to recycled peridotite compositions. The more the material is depleted, the higher its solidus and the higher could be the CMB temperature. The material that lies on the CMB could also be of a different nature, which we discuss below. Anyhow, it is very possible that the mantle geotherm reaches ~3950 K at the CMB, given the strong temperature increase when approaching the CMB. Then, a local enrichment in incompatible and/or volatile elements could depress the mantle solidus by several 100 K and induce melting in specific regions, producing the ultra-low velocity zones (Yu and Garnero, 2018). The nature of the chemical heterogeneities remains uncertain. Many of the incompatible elements, such as Na and K, may have a moderate effect on the solidus temperature, as they can be incorporated into the structure of Dvm (Corgne et al., 2005; Irifune, 1994). In contrast, H₂O could depress the mantle solidus significantly, possibly down to 3400-3500 K if we assume that water explains the difference between our study and the previous experimental works (Kim et al., 2020; Nomura et al., 2014). Finally, the melting of basalt was reported at a temperature of 3600 K (corrected from (Andraut et al., 2014) for wavelength-dependent $\epsilon(\lambda)$), which is slightly lower than the melting point of the mantle. Altogether, this brackets the CMB temperature between 3600 and 3950 K, or between 3400-3500 and 3950 K, if melting of e.g. pyrolytic in ULVZ is triggered by a high concentration of incompatible elements, or water, respectively.

546 **Acknowledgments:** We thank P.D. Asimow, K.K.M. Lee and an anonymous reviewer for their thoughtful
547 comments. This research was financed by the French Government Laboratory of Excellence initiative
548 n°ANR-10-LABX-0006, the French ANR project EquipEx GENESIS (ANR-11-EQPX-0020), the Région
549 Auvergne and the European Regional Development Fund. This is Laboratory of Excellence ClerVolc
550 contribution N°XX.

551

552

553 **References cited:**

554

555 Akins, J.A., Ahrens, T.J., 2002. Dynamic compression of SiO₂: A new interpretation. *Geophys. Res. Lett.* 29,
556 1394.

557 Akins, J.A., Luo, S.N., Asimow, P.D., Ahrens, T.J., 2004. Shock-induced melting of MgSiO₃ perovskite and
558 implications for melts in Earth's lowermost mantle. *Geophys. Res. Lett.* 31, L14612.

559 Andraut, D., Bolfan-Casanova, N., Bouhifd, M.A., Boujibar, A., Garbarino, G., Manthilake, G., Mezouar,
560 M., Monteux, J., Parisiades, P., Pesce, G., 2017. Toward a coherent model for the melting behavior of the
561 deep Earth's mantle. *Phys. Earth Planet. Inter.* 265, 67-81.

562 Andraut, D., Bolfan-Casanova, N., Lo Nigro, G., Bouhifd, M.A., Garbarino, G., Mezouar, M., 2011.
563 Melting curve of the deep mantle applied to properties of early magma ocean and actual core-mantle
564 boundary. *Earth Planet. Sci. Lett.* 304, 251-259.

565 Andraut, D., Morard, G., Garbarino, G., Mezouar, M., Bouhifd, M.A., Kawamoto, T., 2020. Melting
566 behavior of SiO₂ up to 120 GPa. *Phys. Chem. Mineral.* 47, 10.

567 Andraut, D., Munoz, M., Bolfan-Casanova, N., Guignot, N., Perrillat, J.P., Aquilanti, G., Pascarelli, S., 2010.
568 Experimental evidence for perovskite and post-perovskite coexistence throughout the whole D'' region.
569 *Earth Planet. Sci. Lett.* 293, 90-96.

570 Andraut, D., Pesce, G., Bouhifd, M.A., Bolfan-Casanova, N., Henot, J.M., Mezouar, M., 2014. Melting of
571 subducted basalt at the core-mantle boundary. *Science* 344, 892-895.

572 Andraut, D., Pesce, G., Manthilake, G., Monteux, J., Bolfan-Casanova, N., Chantel, J., Novella, D., Guignot,
573 N., King, A., Itie, J.-P., Hennem, L., 2018. Deep and persistent melt layer in the Archaean mantle. *Nat.*
574 *Geosci.* 11, 139-+.

575 Andraut, D., Pison, L., Morard, G., Garbarino, G., Mezouar, M., Bouhifd, M.A., Kawamoto, T., 2022.
576 Comment on: Melting behavior of SiO₂ up to 120 GPa (Andraut et al. 2020). *Phys. Chem. Mineral.* 49, 3.

577 Anzellini, S., Dewaele, A., Mezouar, M., Loubeyre, P., Morard, G., 2013. Melting of Iron at Earth's Inner
578 Core Boundary Based on Fast X-ray Diffraction. *Science* 340, 464-466.

579 Asimow, P.D., 2018. Chapter 15 - Melts Under Extreme Conditions From Shock Experiments, in: Kono, Y.,
580 Sanloup, C. (Eds.), *Magma Under Pressure*. Elsevier, pp. 387-418.

581 Boujibar, A., Bolfan-Casanova, N., Andraut, D., Bouhifd, M.A., Trcera, N., 2016. Incorporation of Fe²⁺ and
582 Fe³⁺ in bridgmanite during magma ocean crystallization. *Am. Miner.* 101, 1560-1570.

583 Catalli, K., Shim, S.H., Prakapenka, V.B., 2009. Thickness and Clapeyron slope of the post-perovskite
584 boundary. *Nature* 462, 782-785.

585 Corgne, A., Liebske, C., Wood, B.J., Rubie, D.C., Frost, D.J., 2005. Silicate perovskite-melt partitioning of
586 trace elements and geochemical signature of a deep perovskitic reservoir. *Geochim. Cosmochim. Acta* 69,
587 485-496.

588 de Koker, N., Karki, B.B., Stixrude, L., 2013. Thermodynamics of the MgO-SiO₂ liquid system in Earth's
589 lowermost mantle from first principles. *Earth Planet. Sci. Lett.* 361, 58-63.

590 de Koker, N., Stixrude, L., 2009. Self-consistent thermodynamic description of silicate liquids, with
591 application to shock melting of MgO periclase and MgSiO₃ perovskite. *Geophys. J. Int.* 178, 162-179.

592 Deng, J., Du, Z., Benedetti, L.R., Lee, K.K.M., 2017. The influence of wavelength-dependent absorption and
593 temperature gradients on temperature determination in laser-heated diamond-anvil cells. *Journal of*
594 *Applied Physics* 121, 025901.

595 Dewaele, A., Belonoshko, A.B., Garbarino, G., Occelli, F., Bouvier, P., Hanfland, M., Mezouar, M., 2012.
596 High-pressure high-temperature equation of state of KCl and KBr. *Phys. Rev. B* 85.

597 Fiquet, G., Auzende, A.L., Siebert, J., Corgne, A., Bureau, H., Ozawa, H., Garbarino, G., 2010. Melting of
598 Peridotite to 140 Gigapascals. *Science* 329, 1516-1518.

599 Fiquet, G., Dewaele, A., Andraut, D., Kunz, M., Le Bihan, T., 2000. Thermoelastic properties and crystal
600 structure of MgSiO₃ perovskite at lower mantle pressure and temperature conditions. *Geophys. Res. Lett.*
601 27, 21-24.

602 Geballe, Z.M., Jeanloz, R., 2012. Origin of temperature plateaus in laser-heated diamond anvil cell
603 experiments. *Journal of Applied Physics* 111, 123518.

604 Giampaoli, R., Kantor, I., Mezouar, M., Boccato, S., Rosa, A.D., Torchio, R., Garbarino, G., Mathon, O.,
605 Pascarelli, S., 2018. Measurement of temperature in the laser heated diamond anvil cell: comparison
606 between reflective and refractive optics. *High Pressure Res* 38, 250-269.

607 Hernlund, J.W., 2010. On the interaction of the geotherm with a post-perovskite phase transition in the deep
608 mantle. *Phys. Earth Planet. Inter.* 180, 222-234.

609 Holtgrewe, N., Greenberg, E., Prescher, C., Prakapenka, V.B., Goncharov, A.F., 2019. Advanced integrated
610 optical spectroscopy system for diamond anvil cell studies at GSECARS. *High Pressure Res* 39, 457-470.

611 Irifune, T., 1994. Absence of an aluminous phase in the upper part of the Earth's lower mantle. *Nature* 370,
612 131-133.

613 Ito, E., Kubo, A., Katsura, T., Walter, M.J., 2004. Melting experiments of mantle materials under lower
614 mantle conditions with implications for magma ocean differentiation. *Phys. Earth Planet. Inter.* 143-144,
615 397-406.

616 Katsura, T., Yoneda, A., Yamazaki, D., Yoshino, T., Ito, E., 2010. Adiabatic temperature profile in the
617 mantle. *Phys. Earth Planet. Inter.* 183, 212-218.

618 Kim, T., Ko, B., Greenberg, E., Prakapenka, V., Shim, S.H., Lee, Y., 2020. Low Melting Temperature of
619 Anhydrous Mantle Materials at the Core-Mantle Boundary. *Geophys. Res. Lett.* 47.

620 Lay, T., Garnero, E.J., Williams, Q., 2004. Partial melting in a thermo-chemical boundary layer at the base
621 of the mantle. *Phys. Earth Planet. Inter.* 146, 441-467.

622 Liebske, C., Frost, D.J., 2012. Melting phase relations in the MgO-MgSiO₃ system between 16 and 26 GPa:
623 Implications for melting in Earth's deep interior. *Earth Planet. Sci. Lett.* 345, 159-170.

624 Litasov, K., Ohtani, E., 2002. Phase relations and melt compositions in CMAS–pyrolite–H₂O system up to
625 25 GPa. *Phys. Earth Planet. Inter.* 134, 105-127.

626 Matas, J., Bass, J.D., Ricard, Y., Mattern, E., Bukowinsky, M.S., 2007. On the bulk composition of the lower
627 mantle: predictions and limitations from generalized inversion of radial seismic profiles. *Geophys. J. Int.*
628 170, 764-780.

629 Mosenfelder, J.L., Asimow, P.D., Frost, D.J., Rubie, D.C., Ahrens, T.J., 2009. The MgSiO₃ system at high
630 pressure: Thermodynamic properties of perovskite, postperovskite, and melt from global inversion of
631 shock and static compression data. *J. Geophys. Res.* 114, B01203.

632 Nabiei, F., 2017. From 2D to 3D Characterization of Materials Subjected to Extreme Pressure and
633 Temperature Conditions. 230.

634 Nabiei, F., Badro, J., Boukaré, C.-É., Hébert, C., Cantoni, M., Borensztajn, S., Wehr, N., Gillet, P., 2021.
635 Investigating Magma Ocean Solidification on Earth Through Laser-Heated Diamond Anvil Cell
636 Experiments. *Geophys. Res. Lett.* 48, e2021GL092446.

637 Nakajima, M., Stevenson, D.J., 2015. Melting and mixing states of the Earth's mantle after the Moon-
638 forming impact. *Earth Planet. Sci. Lett.* 427, 286-295.

639 Nomura, R., Hirose, K., Uesugi, K., Ohishi, Y., Tsuchiyama, A., Miyake, A., Ueno, Y., 2014. Low Core-
640 Mantle Boundary Temperature Inferred from the Solidus of Pyrolite. *Science* 343, 522-525.

641 Nomura, R., Ozawa, H., Tateno, S., Hirose, K., Hernlund, J.W., Muto, S., Ishii, H., Hiraoka, N., 2011. Spin
642 crossover and iron-rich silicate melt in the Earth's deep mantle. *Nature* 473, 199-202.

643 Ohnishi, S., Kuwayama, Y., Inoue, T., 2017. Melting relations in the MgO-MgSiO₃ system up to 70 GPa.
644 *Phys. Chem. Mineral.* 44, 445-453.

645 Ozawa, K., Anzai, M., Hirose, K., Sinmyo, R., Tateno, S., 2018. Experimental Determination of Eutectic
646 Liquid Compositions in the MgO-SiO₂ System to the Lowermost Mantle Pressures. *Geophys. Res. Lett.*
647 45, 9552-9558.

648 Petitgirard, S., Malfait, W.J., Sinmyo, R., Kuppenko, I., Hennem, L., Harries, D., Dane, T., Burghammer, M.,
649 Rubie, D.C., 2015. Fate of MgSiO₃ melts at core–mantle boundary conditions. *Proceedings of the*
650 *National Academy of Sciences* 112, 14186-14190.

651 Pierru, R., Andrault, D., Manthilake, G., Monteux, J., Devidal, J.L., Henry, L., Guignot, N., King, A., 2022.
652 Mantle origin of ancient large igneous provinces. Submitted.

653 Ringwood, A.E., 1975. Pyrolite and the Chondritic Earth Model, in: GrawHill, M. (Ed.), *International series*
654 *in the Earth's and Planetary Sciences*, pp. 189-194.

655 Schultz, E., Mezouar, M., Crichton, W., Bauchau, S., Blattmann, S., Andrault, D., Fiquet, G., Boehler, R.,
656 Rambert, N., Sitaud, B., Loubeyre, P., 2005. Double-sided laser heating system for in situ high pressure-
657 high temperature monochromatic x-ray diffraction at the ESRF. *High Pressure Res* 25, 71-83.

658 Shen, G., Lazor, P., 1995. Measurement of melting temperatures of some minerals under lower mantle
659 conditions. *J. Geophys. Res.* 100, 17699-17713.

660 Simon, F., Glatzel, G., 1929. Fusion-pressure curve. *Zeitschrift für anorganische und allgemeine Chemie* 178,
661 309-316.

662 Stixrude, L., de Koker, N., Sun, N., Mookherjee, M., Karki, B.B., 2009. Thermodynamics of silicate liquids
663 in the deep Earth. *Earth Planet. Sci. Lett.* 278, 226-232.

664 Stixrude, L., Karki, B.B., 2005. Structure and freezing of MgSiO₃ liquid in the Earth's lower mantle. *Science*
665 310, 297-299.

666 Tateno, S., Hirose, K., Ohishi, Y., 2014. Melting experiments on peridotite to lowermost mantle conditions. *J.*
667 *Geophys. Res.* 119, 4684-4694.

668 Tateno, S., Hirose, K., Sata, N., Ohishi, Y., 2009. Determination of post-perovskite phase transition
669 boundary up to 4400 K and implications for thermal structure in D " layer. *Earth Planet. Sci. Lett.* 277,
670 130-136.

671 Tauzin, B., Debayle, E., Wittlinger, G., 2010. Seismic evidence for a global low-velocity layer within the
672 Earth's upper mantle. *Nat. Geosci.* 3, 718-721.

673 Thomson, A.R., Walter, M.J., Lord, O.T., Kohn, S.C., 2014. Experimental determination of melting in the
674 systems enstatite-magnesite and magnesite-calcite from 15 to 80 GPa. *Am. Miner.* 99, 1544-1554.

675 Tronnes, R.G., Frost, D.J., 2002. Peridotite melting and mineral–melt partitioning of major and minor
676 elements at 22–24.5 GPa. *Earth Planet. Sci. Lett.* 197, 117-131.

677 Usui, Y., Tsuchiya, T., 2010. Ab Initio Two-Phase Molecular Dynamics on the Melting Curve of SiO₂. *J.*
678 *Earth Sci.* 21, 801-810.

679 Yu, S.L., Garnero, E.J., 2018. Ultralow Velocity Zone Locations: A Global Assessment. *Geochem.,*
680 *Geophys., Geosyst.* 19, 396-414.

681 Zerr, A., Bohler, R., 1993. Melting of (Mg,Fe)SiO₃-perovskite to 625 kbar: Indication of a high melting
682 temperature in the lower mantle. *Science* 262, 553–555.

683 Zerr, A., Diegeler, A., Bohler, R., 1998. Solidus of earth's mantle. *Science* 281, 243-246.

684

1
2 **Solidus melting of pyrolite and bridgmanite: implication for**
3 **the thermochemical state of the Earth's interior**

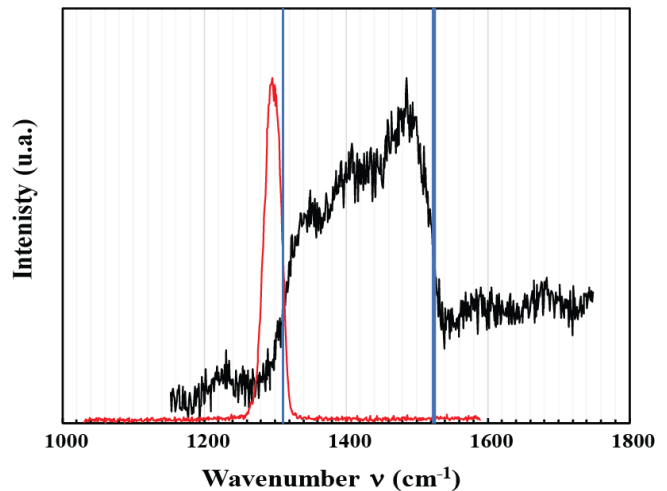
4
5 **Rémy PIERRU**¹, **Laure PISON**¹, **Antoine MATHIEU**¹, **Emmanuel GARDES**^{1,2}, **Gaston**
6 **GARBARINO**³, **Mohamed MEZOUAR**³, **Louis HENNET**⁴ and **Denis ANDRAULT**^{1,‡}
7
8
9

10 **Supplementary material caption:** The supplementary material contains several figures:

- 11 - Suppl. Fig. 1: Pressure measurement using Raman spectroscopy
12 - Suppl. Fig. 2: LH-DAC experimental set-up developed at the LMV
13 - Suppl. Fig. 3: Investigation of the uncertainty of temperature measurement
14 - Suppl. Fig. 4: Series of thermal emission spectra recorded up to the solidus
15 temperature
16 - Suppl. Fig. 5: Typical laser power vs temperature plateaus
17
18
19
20

21 **Supplementary Figures**

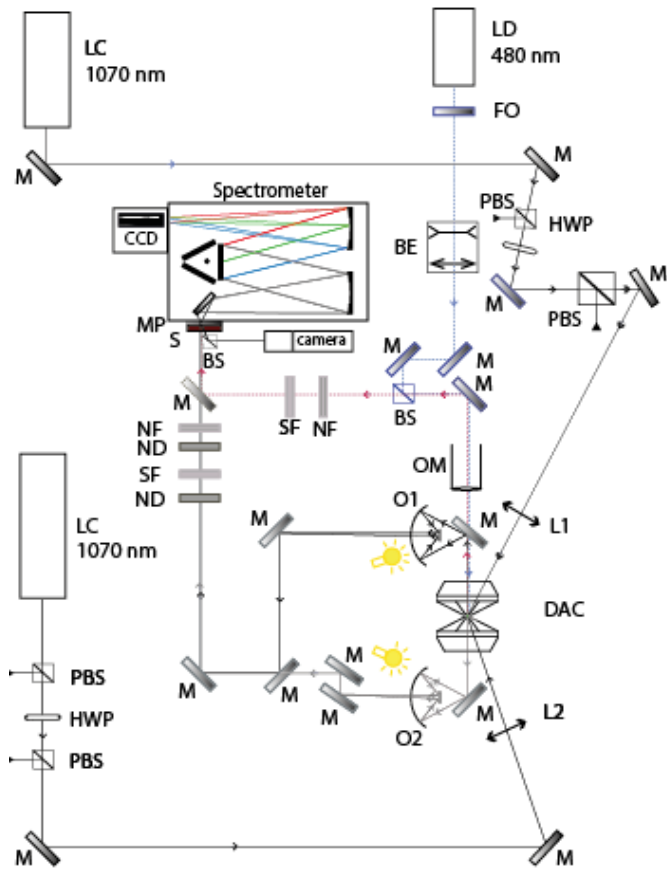
22
23
24 **Suppl. Fig. 1: Pressure measurement using**
25 **Raman spectroscopy.** Pressure is calculated from
26 the shift of the inflection point (blue lines) of
27 Raman spectrum recorded at room (red) and high
28 (black) pressure. Raman spectra are recorded on the
29 surface of the diamond culet as close as possible
30 from the sample. In this example, the inflection
31 point shifts from 1310.8 +/-0.5 cm⁻¹ and 1524.5 +/-
32 2.0 cm⁻¹ yielding a nominal pressure (at 300K) of
33 108.7 +/- 2.5 GPa.
34



35
36
37
38
39
40
41
42
43
44
45
46

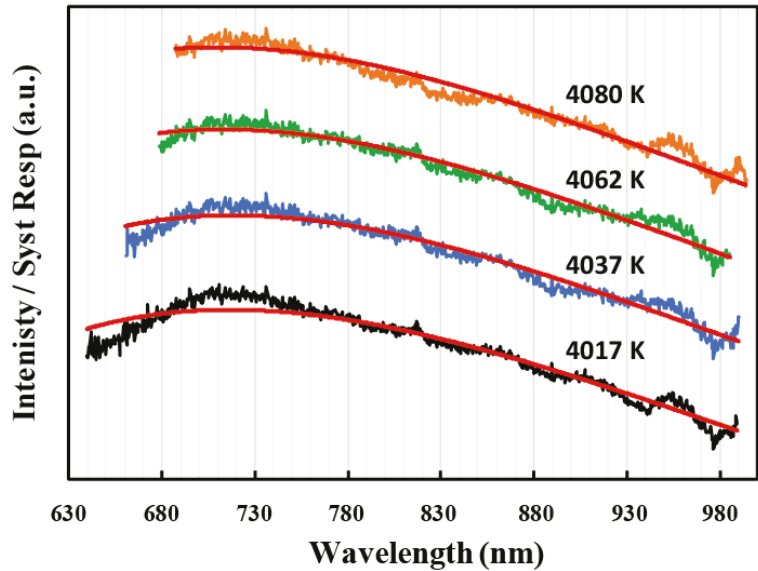
Suppl. Fig. 2: LH-DAC experimental set-up developed at the LMV. Main components are the water-cooled diamond anvil cell, two fiber lasers focused on the compressed sample with an angle of ~ 15 degrees, two reflective Schwarzschild objectives, a camera to visualize the laser spots on both sample sides and a spectrometer to determine the sample pressure and temperature on both sides simultaneously.

LC : Yb Fiber Laser, 100W	Spectrometer: double grating
LD : Diode Laser, 200mW	CCD: camera
DAC : Diamond Anvil Cell	MP : Mirror with Pinholes
O1- 2 : Reflective objective	S : External Shutter
OM : HR Reflective objective	L : Convex Lens: f=50 or 75mm
BS : Beam Splitter 50/50	FO : Clean-up Filter
PBS : Polarized Beam Splitter	SF : Short range pass Filter
HWP : Half-Wave Plate	NF : Notch Filter
BE : Beam Expander	ND : Neutral Density Filter
M : Mirrors	Camera : with Zoom



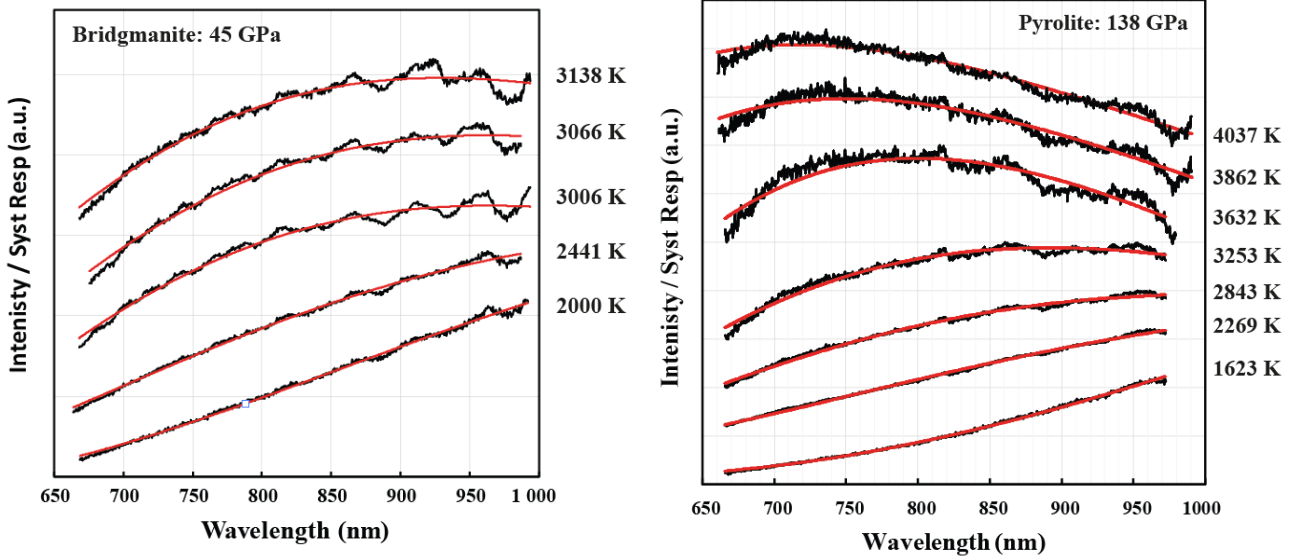
47
48
49
50
51
52
53
54
55
56
57
58
59
60
61
62
63
64
65
66
67
68
69
70
71
72
73
74
75
76
77

Suppl. Fig. 3: Investigation of the uncertainty of temperature measurement. A same thermal emission spectrum recorded at the solidus of pyrolite at ~ 138 GPa is fitted using 4 different ranges of wavelengths: from 640, 660, 680 or 700 nm to ~ 990 nm. The 4 adjustments yield temperatures between 4017 and 4080 K. The best fit is obtained when using the narrowest range of wavelengths; however, the fit quality may be misleading. When using a wider range of wavelengths, the quality of the fit is degraded due to a lower signal intensity at wavelengths shorter than ~ 700 nm. This effect could arise from a stronger interaction between light and electrons at high light energies, inducing a relatively low sample emissivity (i.e. high sample absorption). Still, this type of effects are not known well and could also affect other regions of the recorded thermal emission spectra. As a compromise, it arises that a sample temperature of 4040 ± 25 K is compatible with the fits performed over a wide range of wavelengths.



78
79
80
81

Suppl. Fig. 4: Series of thermal emission spectra recorded up to the solidus temperature: (a) Bridgmanite at 45 GPa (b) Pyrolite at 138 GPa.



82
83
84
85
86
87
88
89
90
91
92
93

Suppl. Fig. 5: Typical laser power vs temperature plateaus: Evolution of the sample temperature with increasing laser power for bridgmanite at 45 GPa and 109 GPa (upper and middle frames) and pyrolite at 138 GPa (lower frame). Temperature remains below the solidus on the plateau; we therefore determine the solidus temperature by averaging the highest temperatures.

